

Geophysical Research Letters



RESEARCH LETTER

10.1029/2024GL109802

Special Collection:

Advancing Interpretable AI/ML Methods for Deeper Insights and Mechanistic Understanding in Earth Sciences: Beyond Predictive Capabilities

Kev Points:

- Physics-based models with interpretable machine learning can identify likely triggering mechanism of earthquakes within an induced sequence
- With this technique, we show that only 22±5% of earthquakes in Paradox Valley are primarily injection-driven
- Injection-driven events have a larger bvalue, are closer to the well, and occur earlier in the injection history

Supporting Information:

Supporting Information may be found in the online version of this article.

Correspondence to:

R. G. Hill, ryleyghill@gmail.com

Citation:

Hill, R. G., Trugman, D. T., & Weingarten, M. (2024). Separating injection-driven and earthquake-driven induced seismicity by combining a fully coupled poroelastic model with interpretable machine learning. *Geophysical Research Letters*, 51, e2024GL109802. https://doi.org/10.1029/2024GL109802

Received 13 APR 2024 Accepted 26 AUG 2024

© 2024. The Author(s).
This is an open access article under the terms of the Creative Commons
Attribution License, which permits use, distribution and reproduction in any medium, provided the original work is properly cited.

Separating Injection-Driven and Earthquake-Driven Induced Seismicity by Combining a Fully Coupled Poroelastic Model With Interpretable Machine Learning

R. G. Hill^{1,2,3}, D. T. Trugman⁴, and M. Weingarten¹

¹Department of Geological Sciences, San Diego State University, San Diego, CA, USA, ²Scripps Institution of Oceanography, University of California San Diego, La Jolla, CA, USA, ³Now at Los Alamos National Laboratory, Los Alamos, NM, USA, ⁴Nevada Seismological Laboratory, University of Nevada, Reno, NV, USA

Abstract In areas of induced seismicity, earthquakes can be triggered by stress changes due to fluid injection and static deformation from fault slip. Here we present a method to distinguish between injection-driven and earthquake-driven triggering of induced seismicity by combining a calibrated, fully coupled, poroelastic stress model of wastewater injection with interpretation of a machine learning algorithm trained on both earthquake catalog and modeled stress features. We investigate seismicity from Paradox Valley, Colorado as an ideal test case: a single, high-pressure injector that has induced thousands of earthquakes since 1991. Using feature importance analysis, we find that injection-driven earthquakes are approximately 22±5% of the total catalog but act as background events that can trigger subsequent aftershocks. Injection-driven events also have distinct spatiotemporal clustering properties with a larger b-value, closer proximity to the well, and earlier occurrence in the injection history. Generalization of our technique can help characterize triggering processes in other regions where induced seismicity occurs.

Plain Language Summary The Paradox Valley Unit, Colorado in the central United States has had a remarkable increase in seismicity coincident with over 8 million cubic meters of brine fluid injection since 1991, inducing thousands of earthquakes within an aquifer 4.5 km below the surface. We use a physics-based model of the Earth combined with statistical and machine learning techniques to help discern which earthquakes are triggered by other earthquakes and which earthquakes are directly triggered by the stress changes from the well as well as their comparative characteristics. Discerning which earthquakes are directly caused from pressure changes due to the fluid injected by the well can inform our understanding of earthquake physics and provide useful information to operators of energy production sites.

1. Introduction

A variety of anthropogenic industrial activities, including wastewater disposal, can induce seismicity (Ellsworth, 2013; Keranen et al., 2014; Shirzaei et al., 2016). Similar to naturally occurring earthquakes, induced seismicity typically occurs on pre-existing, critically stressed faults (Townend & Zoback, 2000). Generating induced seismicity from the reactivation of faults is attributed to several physical mechanisms, including pore pressure diffusion (Keranen & Weingarten, 2018; Langenbruch et al., 2018; Weingarten et al., 2015), poroelastic coupling (Segall & Lu, 2015), and stress changes caused by seismic or aseismic fault slip (Brown & Ge, 2018; Ge & Saar, 2022).

These physical mechanisms for induced seismicity jointly contribute to the triggering potential of each earth-quake. Since induced earthquakes can be triggered by small stress changes of order 1–10 kPa (Bachmann et al., 2012; Cacace et al., 2021; Stokes et al., 2023), a large difficulty arises in deciphering which mechanism was responsible for triggering each earthquake. We are particularly interested in discerning which earthquakes were more likely driven by injection-related stress changes versus those more likely driven by stress changes from prior earthquakes. Furthermore, site-to-site differences in physical rock properties, reservoir structure, fault geometry, and remnant tectonic stress could contribute to differences in the ratio of injection-driven and earthquake-driven events despite similar injection-related stresses.

Relative stress changes from fluid injection require analytical or numerical models to resolve the spatio-temporal evolution of pore pressure and poroelastic stress. To capture the fully coupled poroelastic stress changes

HILL ET AL.

(Biot, 1941; Rice & Cleary, 1976; Wang, 2000) induced from the fluid sources requires detailed knowledge of the hydrogeologic properties of the region. The fault geometry is also critical for resolving fault plane stress tractions that characterize fault stability and the potential for induced seismicity (G. C. P. King et al., 1994; Cocco & Rice, 2002; Levandowski et al., 2018). Hence, any attempt at discerning induced earthquakes requires an accurate and comprehensive hydrogeological model, detailed injection well data, precise fault geometries, and high-resolution earthquake catalog.

Here, we investigate which earthquakes are more likely triggered by stress changes from injection and which earthquakes are more likely triggered by earthquake-earthquake interaction. We built a three-dimensional (3D) fully coupled poroelastic model of Paradox Valley Unit, CO (PVU) to resolve time-dependent pore pressure and stress changes due to brine injection. To inform the contribution of our earthquake triggering mechanisms, we use a random forest regression machine learning analysis trained on Paradox Valley seismicity and SHapley Additive exPlanations (SHAP), a game theoretic approach to explain and interpret the output of machine learning models (Lundberg & Lee, 2017). We compare our results with independent tests of seismicity clustering, which corroborate that the physics-based machine learning method provides insight into discerning triggering mechanism not previously captured. This model explores the induced earthquake triggering process for wastewater disposal and could help distinguish regions that are more or less susceptible to stress changes from anthropogenic sources with applicability to other types of subsurface injection including CO₂ sequestration, enhanced geothermal systems, and hydraulic fracturing.

2. Paradox Valley Unit (PVU) Data

The PVU is a program run by the U.S. Bureau of Reclamation, which has been disposing deep brine into a confined aquifer between 4.3 and 4.6 km depth in Paradox Valley, Colorado since 1995 (Ake et al., 2005; Denlinger & RH O'Connell, 2020) (Figure 1). The high-pressure fluid injection has been associated with >7,000 earthquakes between 1991 and 2012, which have all been documented as induced seismicity (Ake et al., 2005; Block et al., 2015; V. M. King et al., 2016; Denlinger & RH O'Connell, 2020). Most seismic events within 5 km of the injection well were induced within the first 10 years of injection and nearly all within the high permeability injection reservoir known as the Leadville formation. This zone is highly pressurized from decades of continuous pumping and dictates the lateral migration of seismicity away from the wellbore. These carefully studied events support the notion of a \sqrt{t} diffusion model for pressurization from the well (Block et al., 2015; V. M. King et al., 2016) (Figure 2). Additional ancillary data also make this an ideal study region: numerous wells that extend into deeper formations than just the Leadville aquifer, 3D seismic tomography, logs of P-wave velocity, density and porosity from the near surface to basement in the injection well, and logging of geologic units in other wells in the area (Denlinger & RH O'Connell, 2020).

Most importantly for our purposes, previous work has already compiled a detailed, fully coupled poroelastic model (Denlinger & RH O'Connell, 2020). This model is given by a grid description of nodes with corresponding parameter values which we validate in our finite element numerical model (Dassault Systemes, 2020) with improved meshing near the well where pressure and stress gradients are highest (see SM Section 1 in Supporting Information S1). Figure 2 includes a plot of the earthquake distribution overlaid on a cross-section of the numerical model mesh.

3. Methods

The core of our methodology relies on the careful development of machine learning features which will represent the contribution of injection-driven stress changes and earthquake-driven stress change for each event in the PVU catalog. Our injection-driven stress feature is resolved using time-dependent pore pressure and stress changes throughout the PVU. Pore pressure and stress perturbations are used to produce von Mises stress features that are physical inputs for the ML/SHAP analysis. To quantify earthquake-driven stress changes, we create a second feature in the ML/SHAP analysis, which we call the "earthquake feature." The earthquake feature is calculated from the stresses produced by prior earthquakes that may have generated stress perturbations large enough to affect the current earthquake. These two feature weights are then trained on the entire PVU catalog to find the optimal weight of each feature for each earthquake in the PVU catalog. SHAP analysis of the ML model's feature weights allow for interpretation of the relative contribution of each feature to each event. We support our

HILL ET AL. 2 of 11

19448007, 2024, 18, Downloaded from https://agupubs.onlinelibrary.wiley.com/doi/10.1029/2024GL109802 by University Of Nevada Reno, Wiley Online Library on [2.1/07/2025]. See the Terms and Condition

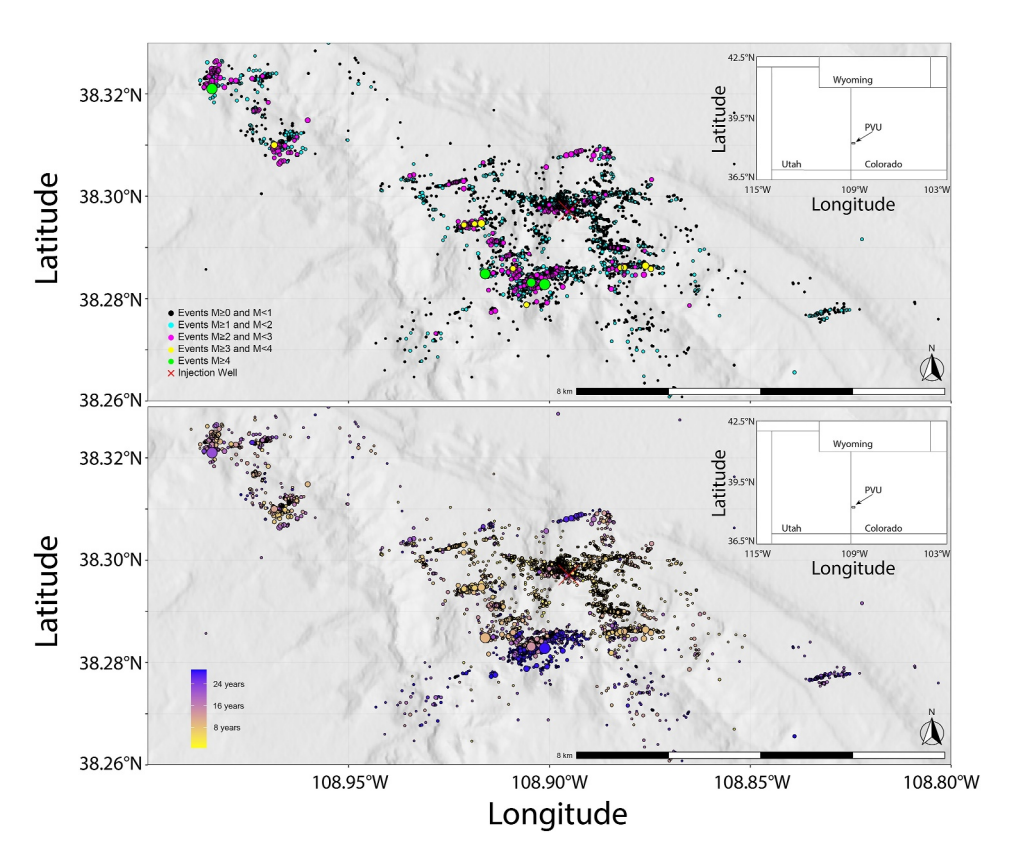


Figure 1. Regional setting of the Paradox Valley Unit, CO (PVU). (a) Earthquakes binned by different magnitude ranges. The well is denoted by the red 'X'. The deep brine injection began in 1991 at a depth of 4.3 km. Most seismicity is clustered near the well, where stress perturbations are largest and fluctuate the most. (b) Temporal evolution of events. There are more than 7,000 earthquakes in the catalog, but we focus our analysis on the 3,000 events occurring within the 8 km radius around the well.

interpretations of triggering mechanisms from the ML/SHAP with results from a nearest neighbor distance cluster analysis.

3.1. Numerical Model

We model the relative increase in pore pressure ΔP (scalar) and poroelastic stress ΔS (second order tensor) for the PVU using a model with one injection well in the center of the model domain (SM Figure 1 in Supporting Information S1). The hydrogeologic structure is based on a nodal distribution of parameters that we reduced down to 1000 unique unit formations and use Abaqus to resolve the linear poroelastic equations (R. G. Hill et al., 2023) (see SM Section 1 in Supporting Information S1). The model dimensions are 50 km by 50 km laterally with a 18 km depth. Figure 2 shows a cross-section through the well injection zone. The injection is divided across three perforated zones consistent with prior modeling and uses the entire injection history as 7,952 unique daily rates in our model from 10-July-1991 to 16-April-2013 (Denlinger & RH O'Connell, 2020) (Figure 2). We output ΔP and ΔS from these daily steps across the entire domain at 284 ~ monthly time steps. We do not include earthquakes in our study that occur outside of the modeled time domain which is restricted by the injection history, although the earthquake catalog does extend until 31-December-2019 (Figure 2).

3.2. Stress Features

The Abaqus outputs of ΔP and ΔS were post-processed in Matlab using abaqus2matlab (Papazafeiropoulos et al., 2017). The stress features of ΔP and ΔS represent the relative change induced from the fluid injection and are resolved at the closest value in the domain to each ~3,000 earthquakes during our study time. We assessed a variety of different stress features during the preliminary stages of this work, consistent with prior studies (DeVries et al., 2018; Qin et al., 2022; Sharma et al., 2020). We found that you Mises stress $(\sqrt{3J_2})$ and you Mises

HILL ET AL. 3 of 11

19448007, 2024, 18, Downloaded from https://agupubs.onlinelibrary.wiley.com/doi/10.1029/2024GL109802 by University Of Nevada Reno, Wiley Online Library on [21/07/2025]. See the Terms

Figure 2. Earthquakes plotted as their radial distance from the well and time. Most earthquakes behave in a typical \sqrt{t} diffusion rate away from the well consistent with progressive lateral migration of seismicity through the permeable Leadville formation (Ake et al., 2005; Block et al., 2015; Denlinger & RH O'Connell, 2020). Flow tests were performed prior to 1995. Notice injection is highest during peak injection rates ~1997. Our model records pore pressure and stress perturbations from 10-July-1991 to 16-April-2013. Numerical model cross section with earthquake and well depth superimposed. The model is a fully coupled poroelastic model based on prior work (Denlinger & RH O'Connell, 2020). We increase the grid discretization near the well to capture large changes in pressure gradients (see SM Section 1 in Supporting Information S1).

stressing rate $(\sqrt{3J_2})$, where J_2 is the second invariant of deviatoric stress, were the best stress-based features for modeling the observed seismicity rate and are the only two stress features we consider hereinafter. We calculate von Mises stress using a strike azimuth of 260° and vertical dip from the dominant azimuth modes of small earthquakes resolved in previous work (Denlinger & RH O'Connell, 2020).

3.3. Earthquake Feature

Static stress transfer modeling can be used to assess earthquake-earthquake triggering on faults embedded in an elastic half space with homogeneous isotropic elastic properties (Lin & Stein, 2004; Toda et al., 2005). Stress transfer can promote or reduce the potential of earthquake triggering, depending on the coefficient of friction, fault geometry, and sense of slip (G. C. P. King et al., 1994; Stein, 1999). Since the exact geometries of every earthquake in our model are unknown, we choose to develop an earthquake feature that is based on the occurrence of prior earthquakes that could have plausibly influenced each earthquake. There are more than 7,000 earthquakes in the catalog, but we focus our analysis on the \sim 3,000 events occurring within the 8 km radius around the well (Figure 1).

We use the 'cutde' package (Thompson, 2021) to resolve elastic stress transfer produced from triangular dislocation element representations of fault slip (Nikkhoo & Walter, 2015). Several assumptions are required for the static stress transfer modeling: (a) We assume a uniform stress drop for every event of 3 MPa, (b) a shear modulus of 30 GPa, and (c) a Poisson ratio of 0.25. Under this framework we show that the von Mises stress is self-similar for both parallel and perpendicular receiver planes at a given distance from the event (SM Figure 2 in Supporting Information S1). By varying event magnitude, we calculate a radius from the center of the dislocation that can increase the potential of failure up to a distance that intersects an assumed 10 kPa triggering threshold (Reasenberg & Simpson, 1992; Stein, 1999). As a sensitivity test we varied the stress drop from 1 to 10 MPa and observe marginal change to the perturbable radius for varying magnitudes (SM Figure 2 in Supporting Information S1). Then, for every earthquake, we create an earthquake-to-earthquake feature, which counts the number of earthquakes that could have perturbed it. The earthquake count is represented by $\ln(N+1)$, where N is the number of perturbing earthquakes to have occurred prior to each event constrained temporally by the number of monthly lags (see Section 3.4). Higher values of this feature indicate a higher likelihood of earthquake-earthquake interaction.

HILL ET AL. 4 of 11

3.4. ML/SHAP Analysis

We use the machine learning technique of random forest regression (RFR) to fit our observed seismicity (Ho. 1998; Ho. 1995). This fit is dissimilar to traditional applications of ML or seismicity forecasts that might split the seismicity into train/test and attempt to forecast the seismicity at a later time. Here, we make no forecast of future seismicity rate. Instead, the RFR makes a fit to the observed seismicity rate and we examine the contribution of features for each model fit. The seismicity rate is calculated as a sum of each earthquake (2,926) for each monthly time step. The earthquakes must be one-hot encoded since the occurrence of an earthquake prior to the other earthquakes is required in the earthquake feature (Section 3.3).

We avoid overfitting and optimize model hyperparameters using an exhaustive grid search applied to a five-fold cross-validation score. The observed seismicity is therefore repeatedly divided into training and test folds with the mean squared error evaluating fit on the test folds which the trained model does not see. The RFR models chosen for our analysis were trained using the hyperparameters derived from the best-performing model during the crossvalidation process.

The input features are composed from the stress and earthquake features as well as their time lags. The time lags are introduced both to capture any potential anisotropy or hydromechanical heterogeneity that are not explicit in the numerical model as well as time delayed effects that former earthquakes or stress history may have when perturbing the current earthquake. We find that including more lags improves the overall fit of our model, up to \sim 50 lags, but is likely over-fitting and unrealistic. We assume that the physical meaning of the lags are unreasonable beyond ~1 year before the actual earthquake timing and reserve our total lags to the local minimum of 5 lags (SM Figure 3 in Supporting Information S1). In other words, a model can contain the current stress/ earthquake feature (+0 lag), the time period prior (+1 lag), and the time periods before that (+2-+5 lag etc.) or any combination of that set (SM Figure 3 in Supporting Information S1).

To assess feature importance, we use SHAP, which provides a robust and self-consistent means to explain the predictions of our target variable (earthquake or no-earthquake) by computing the contribution of each feature to the prediction (Lundberg & Lee, 2017; Shapley, 1953). Larger SHAP values for a given feature, averaged across the data set, signify a higher importance for the model's prediction. A key advantage of SHAP lies in its ability to consistently untangle the impacts of multiple correlated input variables (Trugman & Ben-Zion, 2023). Since SHAP values are by design additive, the contributions of individual features can be summed to describe the contribution that the stress features in aggregate have compared to the earthquake features.

3.5. Cluster Analysis

As an independent test of earthquake behavior, we investigate how the PVU seismicity is distributed in magnitude, space, and time using a traditional cluster analysis. We use the nearest neighbor distance (NND) in the space-time-magnitude domain (Baiesi & Paczuski, 2004) for each pair of events i and j using the following equation:

$$\eta_{ij} = \begin{cases} t_{ij} (r_{ij})^d 10^{-bm_i}, & t_{ij} > 0; \\ \infty, & t_{ij} \le 0 \end{cases}$$
 (1)

Where, t_{ij} is the interevent time (year), r_{ij} is the inter event distance (km), d is the dimension of the earthquake hypocenter distribution (d = 1.32) determined using a box-counting procedure (Corral, 2003) (SM Figure 4 in Supporting Information S1), b is the b-value (b = 0.75) determined by maximum likelihood estimation (Aki, 1965), and m_i is the *i*th event magnitude (Schoenball et al., 2015; Zaliapin & Ben-Zion, 2013). The NND is separable into rescaled distance (R_{ii}) and rescaled time (T_{ii}) where (Zaliapin & Ben-Zion, 2013; Zaliapin et al., 2008):

$$\eta_{ii} = R_{ii}T_{ii} \tag{2}$$

$$\eta_{ij} = R_{ij}T_{ij}$$
(2)
$$R_{ij} = (r_{ij})^d 10^{-bm/2}$$
(3)

HILL ET AL. 5 of 11

$$T_{ii} = (r_{ii})^d 10^{-bm_i/2}, (4)$$

An advantage of this form of NND is that the clustering style of seismicity can be displayed by a joint 2D distribution of rescaled time $\log_{10}T_{ij}$ and rescaled distance $\log_{10}R_{ij}$ (Zaliapin & Ben-Zion, 2013, 2016; Zaliapin et al., 2008). The distribution helps to describe the type of earthquake clustering style, since observed seismicity often shows a bimodal joint distribution divided by a constant line and chosen nearest-neighbor threshold n_0 . Events below this threshold are classified as clustered (i.e., earthquake-driven triggering) and the events that are above this threshold are classified as background (i.e., either injection-driven or independent) (Zaliapin & Ben-Zion, 2016). We use the NND distributions for the PVU as an independent test of the physical mechanism driving each earthquake in the sequence. We hypothesize that our ML/SHAP model will preferentially separate injection-driven versus earthquake-driven events as identified by Zaliapin and Ben-Zion (2016).

4. Results

4.1. Numerical Model Results

The fully coupled poroelastic model shows that areas with seismicity experience pore pressure increases from 0.005 to 9 MPa. Most pore pressure increases occur within an 8 km radius around the injection well (SM Figures 6–11 in Supporting Information S1). Most seismicity occurs in close vicinity of the injection well and the ΔP is highest in early 1999 (9 MPa). The pressure changes near the well mimic injection rate changes as the temporal delay of diffusion is negligible. Elsewhere, the diffusion process dominates the pressure changes and therefore the increase in pore pressure is more gradual through time (SM Figures 9–10 in Supporting Information S1). Across the domain, seismicity occurs during the highest rates of pressure increase. This observation is consistent with other instances of wastewater induced seismicity (Langenbruch et al., 2018; Qin et al., 2022). The increasing pore pressure diffuses laterally through the highly permeable Leadville formation. Low permeability confining units above and below the reservoir restrict vertical pressure migration (Movie S1).

4.2. Cluster Analysis Results

Results of the NND cluster analysis show that a larger portion of the earthquakes are classified as the background mode (Goebel et al., 2019; Zaliapin & Ben-Zion, 2016) (Figure 3a). The constant threshold value $\eta_0 = -4.9$ is chosen based on a 1D Gaussian mixture model analysis (Zaliapin & Ben-Zion, 2016; Zaliapin et al., 2008) (SM Figure 5 in Supporting Information S1). The clustering behavior is similar to other cases of wastewater induced seismicity (Glasgow et al., 2021; Zaliapin & Ben-Zion, 2016). There is a larger population of background events and clustered events occur at short space-time distances. These results are also dissimilar from other cases of induced seismicity that have a more clear bimodal distribution, albeit different mechanical processes are occurring (Zaliapin & Ben-Zion, 2016, e.g., Coso and Salton Sea geothermal areas). A small portion of the background domain is characterized by low R_{ij} and large T_{ij} , which often characterizes these events as repeaters (Hsu et al., 2024; Zaliapin & Ben-Zion, 2016). These events make sense in the context of single well injection. The start-stop nature of the injection means repetitive changes in stress occur at the same locations. This is observed in the pore pressure results at different clusters near the well where the pore pressure closely follows the flux of the injection (SM Figures 6–7 in Supporting Information S1).

4.3. ML/SHAP Model Results

Our preferred model uses the following: 1,000 total trees, a maximum depth of 10, a minimum sample split of 10, and a minimum of four samples for a leaf node. Figure 4a shows the fit of our random forest model for two different model types. One model uses only the von Mises stress rate and earthquake feature (orange) while the other model uses both the von Mises stress and the von Mises stressing rate as well as the earthquake feature (including lags) (green-dashed). Respectively, the models have (12,18) features (~9 million, ~14 million), data points, and 813,428 outputs which are summed over the earthquakes (2,926) for each time step (278) to resolve overall seismicity rate at each time step. We find that the mean squared error (MSE) is slightly lower for the model that includes both stress features. However, we choose to present the parsimonious solution of one stress feature and refer the reader to the supplementary for the results including both stress features, which contains small differences to the main results (SM Figures 12–14 in Supporting Information S1).

HILL ET AL. 6 of 11

19448007, 2024, 18, Downloaded from https://agupubs.onlinelibrary.viley.com/doi/10.1029/2024GL109802 by University Of Nevada Reno,

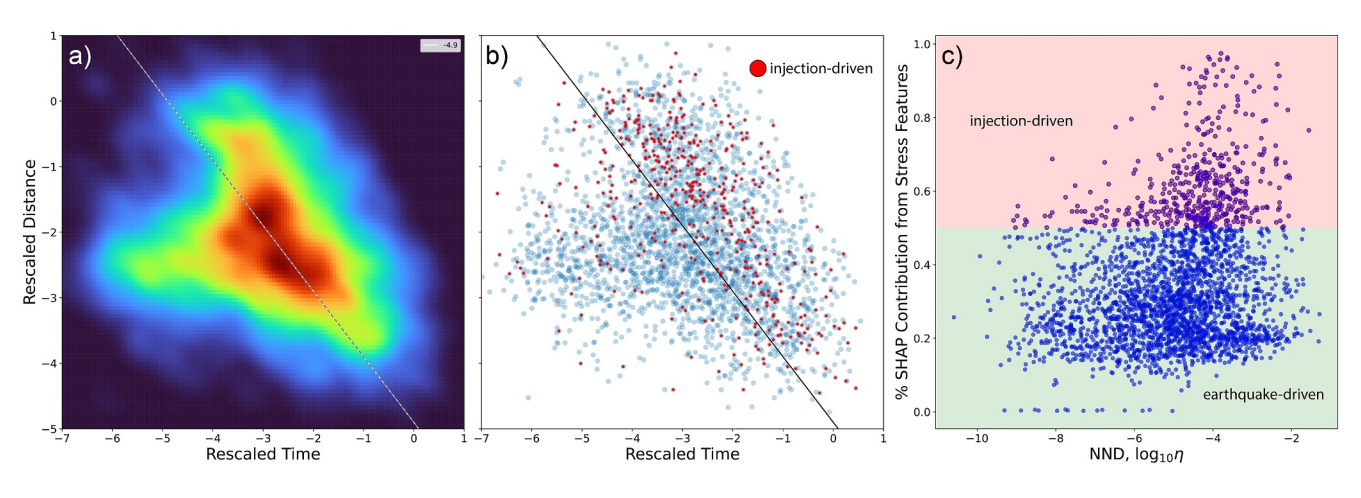


Figure 3. (a) Nearest neighbor time-distance distributions for seismicity in the PVU. The color bar represents the number of event pairs. The total number of earthquakes used in this analysis is 2927. The diagonal dashed line is the η_0 background (above) and clustered (below) mode threshold. The value is a constant distance threshold determined by the 1D Gaussian mixture model and is -4.9. (b) Comparing the earthquakes that have at least 50% stress feature contribution on the rescaled distance rescaled time plot. Many of the earthquakes cluster in the independent background mode with a second distribution toward the repeater mode and a few earthquakes spread out in the cluster mode. (c) The SHAP stress feature contribution versus the nearest neighbor distance value. Many of the earthquakes cluster below the 50% stress feature contribution indicating less injection-driven influence and more earthquake-driven influence. However, earthquakes that have >50% stress feature contribution, denoted as red circles, tends to populate the 'background' mode of the NND (to the right of -4.9). These results are consistent for earthquakes driven by stress from injection since they act as initial parent earthquakes that trigger subsequent seismicity in a region that has experienced stress changes high enough to initiate seismicity.

The SHAP analysis results are summarized in SM Figure 16 in Supporting Information S1. We output the results exclusively at the time when the earthquakes occur since we are only interested in discerning the contribution of the stress features at that time. A summary of the SHAP contributions for all time, not just when the earthquakes occur, is presented in the supplementary material (SM Figure 17 in Supporting Information S1). The feature with the highest overall impact on the model is the perturbable earthquake feature. It represents all earthquakes that potentially perturbed the earthquake in question. The next most important features, with nearly equal importance, are the lagged von Mises stress rates. These stress features are considerably less important on average compared with the earthquake feature.

To assess the total contribution of the stress features versus the earthquake features, we compare the cumulative feature results. Separating which earthquakes are dominated by cumulative feature importance, Figure 4e shows that the ratio of earthquakes that have a higher stress feature contribution compared to earthquakes that have a higher total earthquake feature contribution is about 1:5. We examined the sensitivity of this since it would be expected that increasing lags may contribute to higher contribution to stress. While the stress contribution does increase for models that include 0,+1,+2 lags, after the model reaches +3 lags, earthquakes that are considered to have a higher total stress contribution increase marginally. For example, from +3 to +5 lags the ratio has a percent increase of only ~0.5% (SM Figure 18 in Supporting Information S1). We do not pursue sensitivity past +5 lags as the SHAP analysis becomes computationally prohibitive with increasing features. It is important to note that when testing increasing lag sensitivity, the overall ratio of the total number of stress features to earthquake features remains the same.

5. Discussion

The ML/SHAP model identifies injection-driven earthquakes (i.e., >50% stress feature contribution) predominantly as background events in the NND model (Figures 3b and 3c). In the NND model, background events are mostly the independent Poisson mode (Zaliapin & Ben-Zion, 2016; Zaliapin et al., 2008). This suggests injection-driven earthquakes often act as parent earthquakes, likely induced by pore pressure and stress changes, triggering further seismicity. These results are further supported by the relative timing of these earthquakes, which often occur at the beginning of injection stages (Figure 4b). We statistically compare injection-driven event distribution to the larger catalog using a two-sample Kolmogorov-Smirnov test, which rejects the null hypothesis of identical distributions with 99% confidence (SM Figure 19 in Supporting Information S1). We also explored two interevent time measures to analyze and compare clustering characteristics between injection-driven and earthquake-driven

HILL ET AL. 7 of 11

19448007, 2024, 18, Downloaded from https://agupubs.onlinelibrary.wiley.com/doi/10.1029/2024G1109802 by University Of Nevada Reno, Wiley Online Library on [21/07/2025]. See the Terms and Conditions (https://onlinelibrary.wiley.com/term

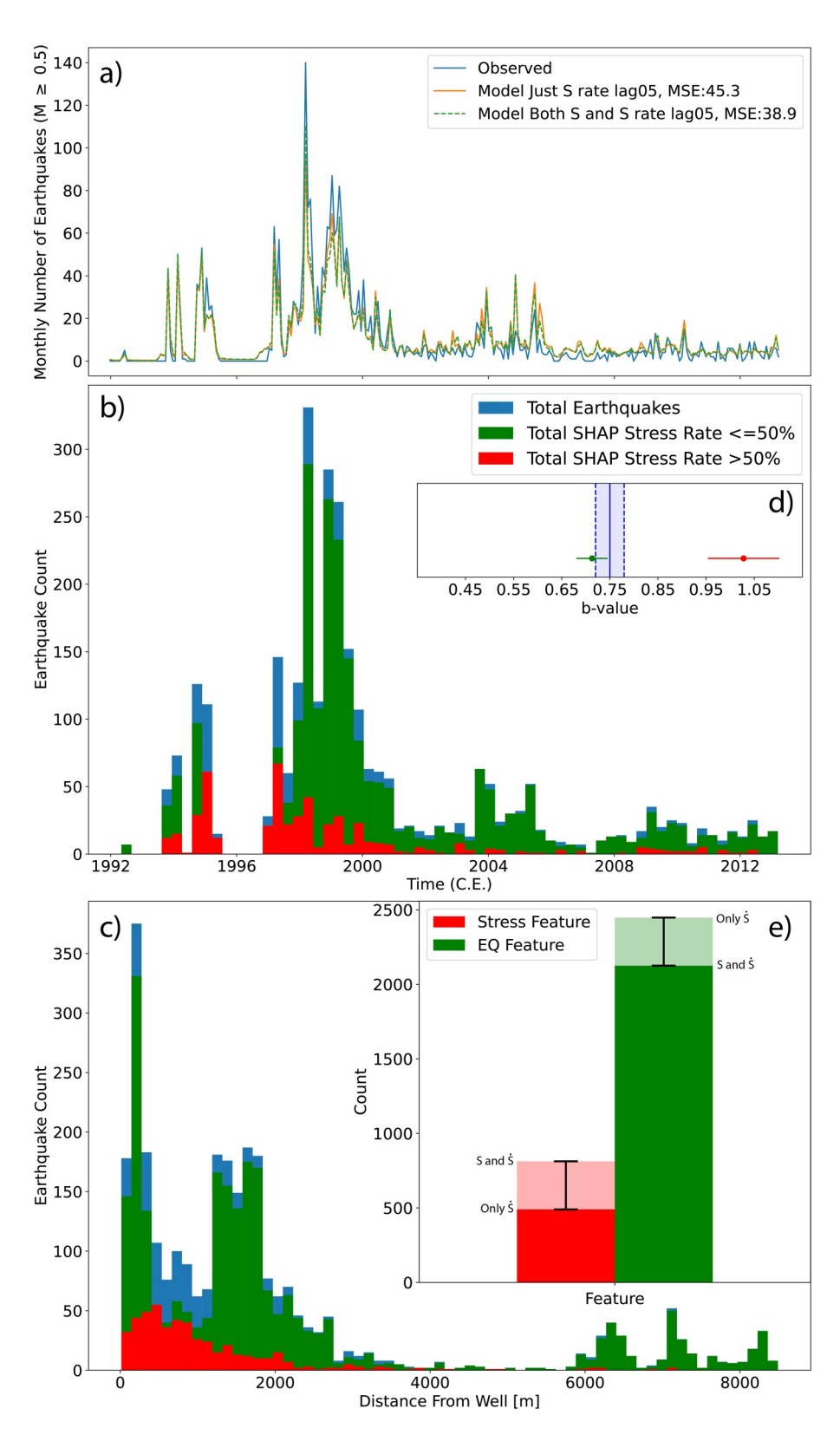


Figure 4.

HILL ET AL. 8 of 11

events (see SM Section 2 in Supporting Information S1). We find that injection-driven earthquakes are less temporally clustered than earthquake-driven events.

We also analyze the spatiotemporal distribution of injection-driven earthquakes (Figures 4b and 4c). They tend to occur earlier in injection history and cluster near the injection well, contrasting with earthquake-driven earthquakes. These events coincide with sharp stress field changes near the well, often preceding clustered seismicity. The b-value of injection-driven earthquakes (Figure 4d) is notably higher (1.03) compared to overall seismicity (0.75) and earthquake-driven events (0.71). This suggests that injection-driven events tend to have lower magnitudes, on average, than the earthquake-driven events and a b-value closer to one indicates that these events may appear to mimic independent background events. The finding that earthquake-driven events produce lower b-values and characterize more of the large events in induced catalogs may have implications for maximum magnitude estimates of induced earthquakes, since initial injection-driven earthquakes at the onset of induced sequences might underestimate the overall maximum magnitude of triggered seismicity.

Clusters of seismic activity away from the well are noticeable, yet they have fewer stress-dominated earthquakes (SM Figure 20 in Supporting Information S1). Often, clusters away from the well are initiated by a few injection-driven earthquakes. This observation is consistent with the machine learning process since earthquakes that had no prior earthquakes would not be expected to have a strong prior earthquake feature contribution. However, not all injection-driven earthquakes precede nearby seismic events. Additionally, areas lacking clear clustering seem to host multiple injection-driven earthquakes, suggesting varied driving mechanisms in those regions (SM Figure 20 in Supporting Information S1).

It is important to recognize that uncertainty is introduced in the model at various stages: physical model material parameters, static stress transfer parameters, RFR input features, and the number of included lags. We affirm the numerical model (see SM Section 1 in Supporting Information S1 and SM Figures 6–11 in Supporting Information S1) and show that the static stress transfer at a triggering threshold of 10 kPa is only marginally sensitive to varied stress drop assumptions (SM Figure 2 in Supporting Information S1). We find that increasing lags beyond +3 does not greatly change the ratio of injection-driven and earthquake-driven earthquakes (SM Figure 18 in Supporting Information S1). The main model sensitivity lies in input features: incorporating von Mises stress and rate increases injection-driven earthquakes from 17% to 27% (Figure 4e and SM Figure 14 in Supporting Information S1). It is unclear whether including both the stress and stress rate features provides a better model since more injection-driven earthquakes also begin to populate the cluster mode, which we assume is a product of overfitting the seismicity rate (Figure 4a and SM Figure 13 in Supporting Information S1). We therefore suggest that these two models serve as lower and upper bound estimates on the number of injection-driven events in the sequence.

Results of this study indicate that the physics-based model, with RFR and SHAP analysis, assigns (490–804) of the 2,926 total earthquakes as injection-driven earthquakes which is only $\sim 30\%$ –50% of independent background mode events determined by the NND cluster analysis. Therefore, not all background mode events are classified as injection-driven. It is important to realize that the independent background mode is not purely a proxy of injection-driven events for NND and additionally the absence of a clear bi-modal distribution in the NND analysis suggests that some events populating the background mode may not have a direct fluid injection influence (Glasgow et al., 2021; Zaliapin & Ben-Zion, 2016). The purpose of the NND analysis is to validate the model results since most of the injection-driven events ($\sim 65\%$ –75%) (SM Figure 13 in Supporting Information S1 and Figure 3b respectively) populate the background mode as expected. We expect this ratio of injection-driven versus earthquake-driven seismicity to vary by geologic region, stress state, distribution of preexisting faults, and injection style. Understanding this ratio is crucial for wastewater management, as it impacts induced seismic hazard. Sites where seismicity is mainly earthquake-driven would be harder to control via well operations best

Figure 4. (a) Seismicity rate observed (blue) and modeled for all time steps. Orange line represents the best fit model that includes only the von-Mises stress rate. The dashed green line includes von-Mises stress and has slightly better fit. (b) Earthquake count (combined total: blue) binned through time for earthquakes with SHAP stress rate <=50% (i.e., earthquake-driven: green) and >50% (i.e., injection-driven: red). (c) same as panel b, but for distance away from well. (d) b-value analysis of all earthquakes (blue), earthquake-driven (green), and injection-driven (red). (e) Ratio of all earthquakes with a larger sum of SHAP value for stress features (red) and the earthquake features (green). We reflect the uncertainty of triggering mechanism based on our two models described in panel (a).

HILL ET AL. 9 of 11

19448007, 2024, 18, Downloaded from https://agupubs

practices, while sites with mostly injection-driven events may be more manageable. Identifying the triggering process in candidate sites can guide energy production decisions, avoiding areas prone to severe triggered seismicity.

6. Conclusion

We separate and interpret earthquake triggering mechanisms using a 3D fully coupled poroelastic model of brine injection and a random forest machine learning model trained on more than 20 years of induced earthquakes at Paradox Valley Unit, Colorado. Combining our random forest model with SHAP analysis of one injection-driven stress feature and one earthquake-driven stress feature helped distinguish each event in the sequence as either more likely injection-driven or more likely earthquake-driven. Our methodology finds that injection-driven earthquakes make up only 22±5% of the catalog and have distinct spatiotemporal clustering with a larger bvalue, closer proximity to the well and earlier occurrence in the injection history. These injection-driven events likely serve to begin the earthquake-driven triggering process which accounts for 78±5% of the earthquakes in the sequence. Comparing our ML/SHAP results with a nearest-neighbor cluster analysis revealed good agreement in stress contribution and cluster style. Our method may be applicable to other regions to help determine the site susceptibility to earthquake triggering.

Data Availability Statement

Data of Abaqus files, post-processing scripts, ML model scripts, and figure generation scripts are available online G. Hill and Ryley, (2024).

The wastewater injection data and earthquake data is available from the Paradox Valley Unit project web page at the Bureau of Reclamation Upper Colorado Basin website (https://www.usbr.gov/uc/progact/paradox/index. html) DOI, 2024.

The numerical models were built and solved using the software Abaqus (Dassault Systemes, 2020).

Acknowledgments

The authors appreciate discussion with RJ Hung and Robert Guyer at early stages of the work. We acknowledge use of the CSRC high-performance computing cluster and other support from San Diego State University. D.T.T acknowledges support from NSF Award EAR-2121666.

References

- Ake, J., Mahrer, K., O'Connell, D., & Block, L. (2005). Deep-injection and closely monitored induced seismicity at paradox valley, Colorado. Bulletin of the Seismological Society of America, 95(2), 664-683. https://doi.org/10.1785/0120040072
- Aki, K. (1965). Maximum likelihood estimate of b in the formula log n= a-bm and its confidence limits. Bull. Earthquake Res. Institute, Tokyo University, 43, 237-239,
- Bachmann, C. E., Wiemer, S., Goertz-Allmann, B., & Woessner, J. (2012). Influence of pore-pressure on the event-size distribution of induced earthquakes. Geophysical Research Letters, 39(9). https://doi.org/10.1029/2012gl051480
- Baiesi, M., & Paczuski, M. (2004). Scale-free networks of earthquakes and aftershocks. Physical Review E, 69(6), 066106. https://doi.org/10. 1103/physreve.69.066106
- Biot, M. A. (1941). General theory of three-dimensional consolidation. Journal of Applied Physics, 12(2), 155-164. Retrieved 2021-04-13, from. https://doi.org/10.1063/1.1712886
- Block, L. V., Wood, C. K., Yeck, W. L., & King, V. M. (2015). Induced seismicity constraints on subsurface geological structure, paradox valley, Colorado, Geophysical Journal International, 200(2), 1172–1195, https://doi.org/10.1093/gij/ggu459
- Brown, M. R., & Ge, S. (2018). Small earthquakes matter in injection-induced seismicity. Geophysical Research Letters, 45(11), 5445-5453. https://doi.org/10.1029/2018g1077472
- Cacace, M., Hofmann, H., & Shapiro, S. A. (2021). Projecting seismicity induced by complex alterations of underground stresses with applications to geothermal systems. Scientific Reports, 11(1), 23560. https://doi.org/10.1038/s41598-021-02857-0
- Cocco, M., & Rice, J. R. (2002). Pore pressure and poroelasticity effects in Coulomb stress analysis of earthquake interactions. Journal of Geophysical Research, 107(B2), 2030. https://doi.org/10.1029/2000jb000138
- Corral, A. (2003). Local distributions and rate fluctuations in a unified scaling law for earthquakes. Physical Review E, 68(3), 035102. https://doi. org/10.1103/physreve.68.035102
- Dassault Systemes. (2020). Abaqus (version 2019). Retrieved from https://www.3ds.com/products/simulia/abaqus
- Denlinger, R. P., & Rh O'Connell, D. (2020). Evolution of faulting induced by deep fluid injection, paradox valley, Colorado. Bulletin of the Seismological Society of America, 110(5), 2308-2327. https://doi.org/10.1785/0120190328
- DeVries, P. M., Viégas, F., Wattenberg, M., & Meade, B. J. (2018). Deep learning of aftershock patterns following large earthquakes. Nature, 560(7720), 632-634. https://doi.org/10.1038/s41586-018-0438-y
- DOI. (2024). Bureau of reclamation (Paradox Valley Unit). [Dataset] Retrieved from https://www.usbr.gov/uc/progact/paradox/index.html. Accessed 10 10 2023
- Ellsworth, W. L. (2013). Injection-induced earthquakes. Science, 341(6142). https://doi.org/10.1126/science.1225942
- Ge, S., & Saar, M. O. (2022). Induced seismicity during geoenergy development—A hydromechanical perspective. Journal of Geophysical Research: Solid Earth, 127(3), e2021JB023141. https://doi.org/10.1029/2021jb023141
- Glasgow, M., Schmandt, B., Wang, R., Zhang, M., Bilek, S. L., & Kiser, E. (2021). Raton basin induced seismicity is hosted by networks of short basement faults and mimics tectonic earthquake statistics. Journal of Geophysical Research: Solid Earth, 126(11), e2021JB022839. https://doi. org/10.1029/2021ib022839

HILL ET AL. 10 of 11

- Goebel, T., Rosson, Z., Brodsky, E., & Walter, J. (2019). Aftershock deficiency of induced earthquake sequences during rapid mitigation efforts in Oklahoma. Earth and Planetary Science Letters, 522, 135–143. https://doi.org/10.1016/j.epsl.2019.06.036
- Hill, G., & Ryley (2024). Data and code for modeling Paradox Valley Unit. [Dataset]. https://doi.org/10.5281/zenodo.10967359. Zenodo
- Hill, R. G., Weingarten, M., Rockwell, T. K., & Fialko, Y. (2023). Major southern San Andreas earthquakes modulated by lake-filling events. Nature, 618, 761–766. https://doi.org/10.1038/s41586-023-06058-9
- Ho, T. K. (1998). The random subspace method for constructing decision forests. IEEE Transactions on Pattern Analysis and Machine Intelligence, 20(8), 832–844. https://doi.org/10.1109/34.709601
- Ho, T. K. (1995). Proceedings of 3rd international conference on document analysis and recognition. In Proceedings of 3rd international conference on document analysis and recognition.
- Hsu, Y.-F., Zaliapin, I., & Ben-Zion, Y. (2024). Informative modes of seismicity in nearest-neighbor earthquake proximities. *Journal of Geophysical Research: Solid Earth*, 129(3), e2023JB027826. https://doi.org/10.1029/2023jb027826
- Keranen, K. M., & Weingarten, M. (2018). Induced seismicity. Annual Review of Earth and Planetary Sciences, 46(1), 149–174. https://doi.org/ 10.1146/annurev-earth-082517-010054
- Keranen, K. M., Weingarten, M., Abers, G. A., Bekins, B. A., & Ge, S. (2014). Sharp increase in central Oklahoma seismicity since 2008 induced by massive wastewater injection. *Science*, 345(6195), 448–451. https://doi.org/10.1126/science.1255802
- King, G. C. P., Stein, R. C., & Lin, J. (1994). Static stress change and the triggering of earthquakes. Bulletin of the Seismological Society of America, 84, 935–953.
- King, V. M., Block, L. V., & Wood, C. K. (2016). Pressure/flow modeling and induced seismicity resulting from two decades of high-pressure
- $Nature\ Communications,\ 9(1),\ 1-10.\ https://doi.org/10.1038/s41467-018-06167-4$ Levandowski, W., Weingarten, M., & Walsh, R., III. (2018). Geomechanical sensitivities of injection-induced earthquakes. $Geophysical\ Research$
- Letters, 45(17), 8958–8965. https://doi.org/10.1029/2018gl077551

 Lin, J., & Stein, R. S. (2004). Stress triggering in thrust and subduction earthquakes and stress interaction between the southern san andreas and
- nearby thrust and strike-slip faults. Journal of Geophysical Research, 109(B2). https://doi.org/10.1029/2003jb002607 Lundberg, S. M., & Lee, S.-I. (2017). A unified approach to interpreting model predictions. Advances in Neural Information Processing Sys-
- Lundberg, S. M., & Lee, S.-I. (2017). A unified approach to interpreting model predictions. Advances in Neural Information Processing Systems, 30.
- Nikkhoo, M., & Walter, T. R. (2015). Triangular dislocation: An analytical, artefact-free solution. *Geophysical Journal International*, 201(2), 1119–1141. https://doi.org/10.1093/gji/ggv035
- Papazafeiropoulos, G., Muñiz-Calvente, M., & Martínez-Pañeda, E. (2017). Abaqus2matlab: A suitable tool for finite element post-processing. Advances in Engineering Software, 105, 9–16. https://doi.org/10.1016/j.advengsoft.2017.01.006
- Qin, Y., Chen, T., Ma, X., & Chen, X. (2022). Forecasting induced seismicity in Oklahoma using machine learning methods. *Scientific Reports*, 12(1), 9319. https://doi.org/10.1038/s41598-022-13435-3
- Reasenberg, P. A., & Simpson, R. W. (1992). Response of regional seismicity to the static stress change produced by the loma prieta earthquake. Science, 255(5052), 1687–1690. https://doi.org/10.1126/science.255.5052.1687
- Rice, J. R., & Cleary, M. P. (1976). Some basic stress diffusion solutions for fluid-saturated elastic porous media with compressible constituents. Review of Geophysics, 14(2), 227–241. Retrieved 2021-04-13, from. https://doi.org/10.1029/RG014i002p00227
- Schoenball, M., Davatzes, N. C., & Glen, J. M. (2015). Differentiating induced and natural seismicity using space-time-magnitude statistics applied to the coso geothermal field. *Geophysical Research Letters*, 42(15), 6221–6228. https://doi.org/10.1002/2015gl064772
- Segall, P., & Lu, S. (2015). Injection-induced seismicity: Poroelastic and earthquake nucleation effects. *Journal of Geophysical Research: Solid Earth*, 120(7), 5082–5103. https://doi.org/10.1002/2015jb012060
- Shapley, L. S. (1953). A value for n-person games.
- Sharma, S., Hainzl, S., Zöeller, G., & Holschneider, M. (2020). Is Coulomb stress the best choice for aftershock forecasting? *Journal of Geophysical Research: Solid Earth*, 125(9), e2020JB019553. https://doi.org/10.1029/2020Jb019553
- Shirzaei, M., Ellsworth, W. L., Tiampo, K. F., González, P. J., & Manga, M. (2016). Surface uplift and time-dependent seismic hazard due to fluid injection in eastern Texas. Science, 353(6306), 1416–1419. https://doi.org/10.1126/science.aag0262
- Stein, R. S. (1999). The role of stress transfer in earthquake occurrence. Nature, 402(6762), 605-609. https://doi.org/10.1038/45144
- Stokes, S. M., Ge, S., Brown, M. R., Menezes, E. A., Sheehan, A. F., & Tiampo, K. F. (2023). Pore pressure diffusion and onset of induced seismicity. *Journal of Geophysical Research: Solid Earth*, 128(3), e2022JB026012. https://doi.org/10.1029/2022jb026012
- Thompson, B. (2021). cutde. Retrieved from https://github.com/tbenthompson/cutde
- Toda, S., Stein, R. S., Richards-Dinger, K., & Bozkurt, S. B. (2005). Forecasting the evolution of seismicity in southern California: Animations built on earthquake stress transfer. *Journal of Geophysical Research*, 110(B5). https://doi.org/10.1029/2004jb003415
- Townend, J., & Zoback, M. D. (2000). How faulting keeps the crust strong. *Geology*, 28(5), 399–402. https://doi.org/10.1130/0091-7613(2000) 028<0399:hfktcs>2.3.co;2
- Trugman, D. T., & Ben-Zion, Y. (2023). Coherent spatial variations in the productivity of earthquake sequences in California and Nevada. *The Seismic Record*, 3(4), 322–331. https://doi.org/10.1785/0320230039
- Wang, H. (2000). Theory of linear poroelasticity: With applications to geomechanics and hydrogeology (p. 287). Princeton Univ. Press.
- Weingarten, M., Ge, S., Godt, J. W., Bekins, B. A., & Rubinstein, J. L. (2015). High-rate injection is associated with the increase in us mid-continent seismicity. *Science*, 348(6241), 1336–1340. https://doi.org/10.1126/science.aab1345
- Zaliapin, I., & Ben-Zion, Y. (2013). Earthquake clusters in southern California i: Identification and stability. *Journal of Geophysical Research:* Solid Earth, 118(6), 2847–2864. https://doi.org/10.1002/jgrb.50179
- Zaliapin, I., & Ben-Zion, Y. (2016). Discriminating characteristics of tectonic and human-induced seismicity. *Bulletin of the Seismological Society of America*, 106(3), 846–859. https://doi.org/10.1785/0120150211
- Zaliapin, I., Gabrielov, A., Keilis-Borok, V., & Wong, H. (2008). Clustering analysis of seismicity and aftershock identification. *Physical Review Letters*, 101(1), 018501. https://doi.org/10.1103/physrevlett.101.018501

HILL ET AL. 11 of 11